subsequent self-coagulation of TSCs is able to grow TSCs to a detectable size. A nucleation rate of 50–100 cm^{-3} s^{-1} is needed to explain the observed number concentrations. As the ionization rate under typical tropospheric conditions is of the order of 1–5 ion pairs cm^{-3} s^{-1} (ref. 25), we can rule out ion-induced nucleation as a probable aerosol formation route. If there exist pathways other than ternary nucleation of H_2SO_4–NH_3–H_2O, they should occur as easily as the ternary one. However, additional condensable vapours will still be required to activate TSCs to detectable sizes and further to cloud condensation nuclei. □

Received 5 July 1999; accepted 10 January 2000.

1. Weber, R. J. *et al.* New particle formation in the remote troposphere: A comparison of observations at various sites. *Geophys. Res. Lett.* **26,** 307–310 (1999).
2. Covert, D. S., Kapustin, V. N., Quinn, P. K. & Bates, T. S. New particle formation in the marine boundary layer. *J. Geophys. Res.* **97,** 20581–20587 (1992).
3. Kulmala, M., Toivonen, A., Mäkelä, J. M. & Laaksonen, A. Analysis of the growth of nucleation mode particles observed in boreal forest. *Tellus* **50,** 449–462 (1998).
4. Korhonen, P. *et al.* Ternary nucleation of H_2SO_4, NH_3, and H_2O in the atmosphere. *J. Geophys. Res.* **104,** 26349–26353 (1999).
5. Clarke, A. D. Atmospheric nuclei in the remote free troposphere. *J. Atmos. Chem.* **14,** 479–488 (1992).
6. Schröder, F. & Ström, J. Aircraft measurements of submicrometer aerosol particles (> 7 nm) in the midlatitude free troposphere and tropopause region. *Atmos. Res.* **44,** 333–356 (1997).
7. Raes, F., Van Dingenen, R., Cuevas, E., Van Velthoven, P. F. J. & Prospero, J. M. Observations of aerosols in the free troposphere and marine boundary layer of the subtropical Northeast Atlantic: Discussion of processes determining their size distribution. *J. Geophys. Res.* **102,** 21315–21328 (1997).
8. Hoppel, W. A., Frick, G. M., Fitzgerand, J. W. & Larson, R. E. Marine boundary layer measurements of new particle formation and the effects nonprecipitating clouds have on aerosol size distribution. *J. Geophys. Res.* **99,** 14443–14459 (1994).
9. Van Dingenen, R., Raes, F. & Jensen, N. R. Evidence for anthropogenic impact on number concentration and sulphate content of cloud-processed aerosol particles over the North Atlantic. *J. Geophys. Res.* **100,** 21057–21067 (1995).
10. Weber, R. J. *et al.* A study of new particle formation and growth involving biogenic trace gas species measured during ACE-1. *J. Geophys. Res.* **103,** 16385–16396 (1998).
11. Clarke, A. D. *et al.* Particle production in the remote marine atmosphere: Cloud outflow and subsidence during ACE 1. *J. Geophys. Res.* **103,** 16397–16409 (1998).
12. O'Dowd, C. *et al.* On the photochemical production of biogenic new particles in the coastal boundary layer. *Geophys. Res. Lett.* **26,** 1707–1710 (1999).
13. Hegg, D. A., Radke, L. F. & Hobbs, P. V. Measurements of Aitken nuclei and cloud condensation nuclei in the marine atmosphere and their relation to the DMS-cloud-climate hypothesis. *J. Geophys. Res.* **96,** 18727–18733 (1991).
14. Wiedensohler, A. *et al.* Occurrence of an ultrafine particle mode less than 20 nm in diameter in the marine boundary layer during Arctic summer and autumn. *Tellus B* **48,** 213–222 (1996).
15. Pirjola, L., Laaksonen, A., Aalto, P. & Kulmala, M. Sulphate aerosol formation in the Arctic boundary layer. *J. Geophys. Res.* **103,** 8309–8322 (1998).
16. Kerminen, V. -M. & Wexler, A. S. Post-fog nucleation of H_2SO_4-H_2O particles in smog. *Atmos. Environ.* **28,** 2399–2406 (1994).
17. Kerminen, V. -M. & Wexler, A. S. The occurrence of sulphuric acid-water nucleation in plumes: Urban environment. *Tellus B* **48,** 65–82 (1996).
18. Mäkelä, J. M. *et al.* Observations of ultrafine aerosol particle formation and growth in boreal forest. *Geophys. Res. Lett.* **24,** 1219–1222 (1997).
19. Easter, R. C. & Peters, L. K. Binary homogeneous nucleation: Temperature and relative humidity fluctuations, nonlinearity, and aspects of new particle production in the atmosphere. *J. Appl. Meteorol.* **33,** 775–784 (1994).
20. Nilsson, E. D. & Kulmala, M. The potential for atmospheric mixing processes to enhance the binary nucleation rate. *J. Geophys. Res.* **103,** 1381–1389 (1998).
21. Doyle, G. J. Self nucleation in the sulphuric acid-water system. *J. Chem. Phys.* **35,** 795–599 (1961).
22. Raes, F., Saltelli, A. & Van Dingenen, R. Modelling formation and growth of H_2SO_4-H_2O aerosols: uncertainty analysis and experimental evaluation. *J. Aerosol Sci.* **23,** 759–771 (1992).
23. Kulmala, M., Laaksonen, A. & Pirjola, L. Parameterizations for sulphuric acid/water nucleation rates. *J. Geophys. Res.* **103,** 8301–8308 (1998).
24. Coffman, D. J. & Hegg, D. A. A preliminary study of the effect of ammonia on particle nucleation in the marine boundary layer. *J. Geophys. Res.* **100,** 7147–7160 (1995).
25. Raes, F. & Janssens, A. Ion-induced aerosol formation in a H_2O-H_2SO_4 system. 1. Extension of the classical theory and search for experimental evidence. *J. Aerosol Sci.* **16,** 217–227 (1985).
26. Stolzenburg, M. R. & McMurry, P. H. An ultrafine aerosol condensation nucleus counter. *Aerosol Sci. Technol.* **14,** 48–65 (1991).
27. Weber, R. J. *et al.* Inversion of ultrafine condensation nucleus counter pulse height distributions to obtain nonaparticle (~3 to 10 nm) size distributions. *J. Aerosol Sci.* **29,** 601–615 (1998).
28. Hörrak. U., Salm, J. & Tammet, H. Bursts of intermediate ions in atmospheric air. *J. Geophys. Res.* **103,** 13909–13915 (1998).
29. Reischl, G. P., Mäkelä, J. M., Karch, R. & Necid, J. Bipolar charging of ultrafine particles in the size range below 10 nm. *J. Aerosol Sci.* **27,** 931–949 (1996).
30. Pirjola, L. Effects of the increased UV radiation and biogenic VOC emissions on ultrafine aerosol formation. *J. Aerosol. Sci.* **30,** 355–367 (1999).

Acknowledgements

We thank R. J. Charlson and C. D. O'Dowd for helpful comments.

Correspondence and requests for materials should be addressed to M. K. (e-mail: markku.kulmala@helsinki.fi).

Geodetic evidence for a low slip rate in the Altyn Tagh fault system

Rebecca Bendick*, Roger Bilham*†, Jeffrey Freymueller‡, Kristine Larson§ & Guanghua Yin‖

* *CIRES & Department of Geological Sciences, University of Colorado, Boulder, Colorado 80309-0399, USA*
† *Earth Sciences, Oxford University, Parks Road, Oxford OX1 3PR, UK*
‡ *Geophysical Institute, PO Box 757320, University of Alaska, Fairbanks, Alaska 99775-7320, USA*
§ *Department of Aerospace Engineering Sciences, University of Colorado, Boulder, Colorado 80309-0429, USA*
‖ *Xinjiang Seismic Bureau, Urumqi, Xinjiang, PRC*

The collision between India and Asia has been simulated with a variety of computational models that describe or predict the motions of the main faults of east Asia. Geological slip-rate estimates of 20–30 mm yr^{-1} suggest that the largest of these faults, the 2,000-km-long Altyn Tagh fault system on the northern edge of the Tibetan plateau, absorbs as much of the Indo-Asian convergence signal as do the Himalayas[1,2]—partly by oblique slip and partly by contraction and mountain growth[3–5]. However, the predictions of dynamic models for Asian deformation[6] and the lower bounds of some geological slip-rates estimates (3–9 mm yr^{-1}; refs 7, 8) suggest that the Altyn Tagh system is less active. Here, we report geodetic data from 89–91° E that indicate left-lateral shear of 9 ± 5 mm yr^{-1} and contraction of 3 ± 1 mm yr^{-1} across the Altyn Tagh system. This result—combined with our finding that, at 90° E, Tibet contracts north–south at 9 ± 1 mm yr^{-1}—supports the predictions of dynamic models of Asian deformation.

In kinematic views of the Indo-Asian plate collision, India's northward motion is absorbed by slip on a small number of active faults bounding major structural units in the collision zone[4,9,10]. The blocks of continental crust between these major faults are usually modelled as elastic; they deform only in the sense that slip on smaller faults within them may permit slow thickening, or other relatively minor, inelastic changes of shape of each block[9,11,12]. In contrast, dynamic models of Asian deformation (models that recognize collisional forces and inferred viscous and elastic properties of the blocks) anticipate deformation throughout the crust and upper mantle[13,14]. Geodetic data provide present-day constraints for these models, both in the form of estimates of the translation, rotation and deformation of crustal blocks, and also in the form of independent estimates of the rate of shear strain applied to intervening faults. The geodetic surveys discussed here lie between longitudes 86° and 92° E across the Altyn Tagh fault and extend southward to India and northward to the Tien Shan. The absence of perturbations to the surface strain-field from recent earthquakes of magnitude $M > 7$ on the Altyn Tagh fault at this longitude permits us to infer the current slip-rate on the fault from the rate of shear strain centred on the fault. Levelling data record relative elevation changes of 57 buried bench-marks spaced at intervals of 4–10 km. Benchmarks north of the Altyn Tagh fault were measured in 1957 and 1979; those south of the fault were measured in 1963 and 1979 (Fig. 1). The Global Positioning System (GPS) data include 13 control points on rock or concrete markers set at variable distances on a 300-km-long linear array across the fault.

The levelling data (Fig. 1) show a maximum uplift rate of 3 mm yr^{-1} near the northern edge of the mountains relative to points in the Tarim basin. Although a short-wavelength vertical-velocity field peaking at 1 mm yr^{-1} is evident on a N30°W fold belt south of the Altyn Tagh fault, no uplift occurs near the fault. We estimate a maximum vertical-velocity uncertainty in these data to be 1–2 mm yr^{-1} (Fig. 2) from a combination of random[15] and systematic

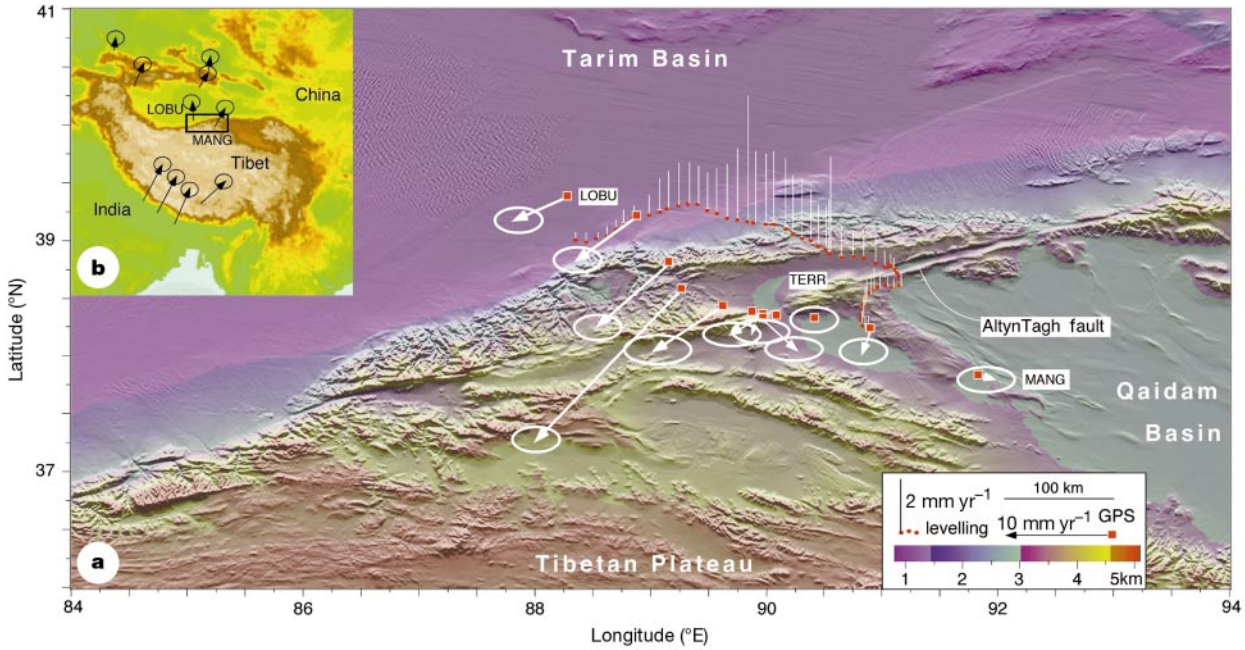

Figure 1 Deformation of the Tibetan plateau. **a**, GPS displacement vectors, and vertical velocities from spirit-level measurements, superimposed on relief map of the northern edge of the Tibetan plateau illuminated from the north. GPS velocity vectors relative to a point (TERR) 5 km south of the Altyn Tagh fault; vertical velocities relative to the southeastern end of the levelling line (see Fig. 2b for uncertainties). **b**, GPS velocities of points between India and Tien Shan relative to Eurasia (largest vector 33 mm yr^{-1}).

errors. The absence of a significant correlation between slope and tilt-rate (Fig. 3) suggests that height-dependent errors are small. The GPS data (Table 1) were obtained as multiple 8-h sessions in 1994 and as multiple 12-h sessions in 1998 using dual frequency GPS receivers. A point at Urumqi (URUR) operated continuously during each survey and a minimum of two local stations were operated concurrently to provide short local baselines. Data from the Altyn Tagh network, plus data from fixed stations at Urumqi, Shanghai and Tsukuba were processed using the GIPSY/OASIS software[16]. Computational uncertainties are approximately ± 2.4 mm yr^{-1} east and ± 1.7 mm yr^{-1} north. With the exception of one outlier (PAXI, that we omit from consideration because its motion exceeds the displacement vectors of four neighbouring points by 2σ), the maximum fault-parallel velocity is 10 mm yr^{-1} in a left-lateral sense relative to the mean position of points southeast of the fault, and the maximum fault-normal horizontal velocity is less than 3 mm yr^{-1}. The measured convergence vector across the Altyn Tagh fault is normal to the strike of east–southeast-trending folds south of the fault.

We assume that aseismic creep at depth is responsible for the observed surface velocity fields. If we assume further that they are generated by creep processes on single dislocations, or on relatively narrow zones of concentrated shear at depth, we may estimate the geometry and rate of slip of these surfaces using elastic dislocation theory[17]. The observed maxima in the vertical and horizontal surface-deformation fields are separated by more than 50 km and we model each field separately. The fault-parallel horizontal-velocity field in Fig. 2 can be emulated by slip on a vertical, buried two-dimensional fault slipping at rates of 9 ± 5 mm yr^{-1} at locking depths of 8–36 km (1σ). The uncertainty in the rate and locking-depth is derived from the weighted misfit of the model to the data (Fig. 4).

The vertical deformation field may be modelled with the same elastic dislocation theory using a reverse fault, sub-parallel to the Altyn Tagh fault dipping southwards. Dislocation geometries that emulate the vertical-velocity field consist of slip at 5 ± 1 mm yr^{-1} on $30 \pm 20°$ SE dipping planar faults with lengths of 30–100 km

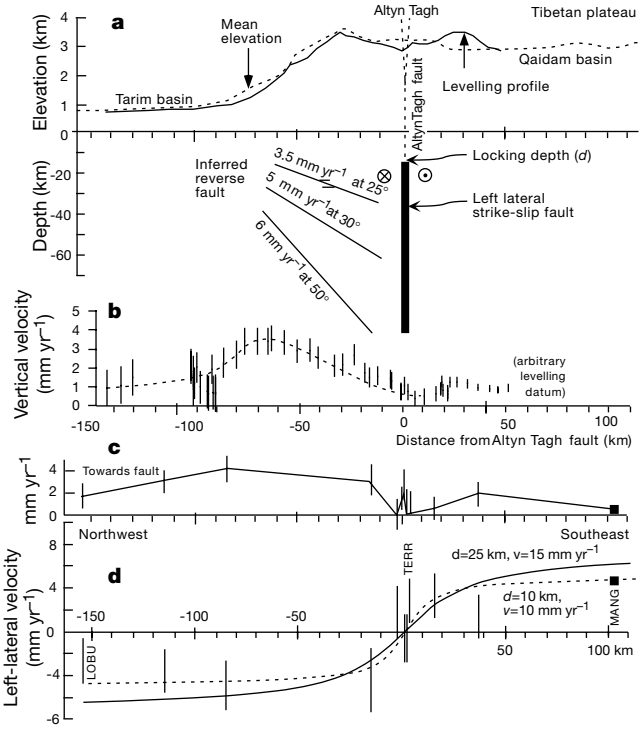

Figure 2 Sections at N10° W across the Altyn Tagh system. **a**, Topographic section normal to the Altyn Tagh fault at 90° E with observed and synthetic velocity fields projected normal to fault. **b**, Vertical velocities from levelling. **c**, Fault-normal velocities. **d**, Fault-parallel velocities from GPS geodesy. Uncertainties in the levelling data are relative to the southeastern end of the line, and uncertainties in the GPS data are shown relative to MANG. A range of inferred dislocation geometries that emulate the vertical velocity field northwest of the Altyn Tagh fault are shown with representative velocities and dips. Satisfactory (1σ) combinations of geometry and slip rate are identified in Fig. 4.

starting at a depth of 10–20 km, and with a surface projection intersecting the northern edge of the mountains. A tradeoff exists between dip and slip-rate such that the range of acceptable models result in 3 ± 1 mm yr^{-1} of surface convergence (Fig. 4), consistent with the observed fault-normal GPS contraction of 2.5 ± 1 mm yr^{-1}. A common feature of these dislocations is that they must terminate down-dip, close to the vertical Altyn Tagh fault. The data are inconsistent with active dislocations that extend south of the Altyn Tagh fault, or with slip on curved surfaces.

A surprising result indicated by the 50-km separation of the maxima in the convergent and strike-slip strain fields, is that strain partitioning occurs aseismically below mid-crustal levels. In some models for partitioning, frictional conditions in the seismogenic crust control the separation of slip into dip-slip and strike-slip components[18,19]. Our data suggest that partitioning processes are not restricted to the brittle crust, but we cannot distinguish between a mechanism where stresses driving aseismic slip are localized here by shallow seismic processes, or whether lower-crust partitioning is responsible for the stress distribution that drives shallow earthquakes. Stresses leading to strain-partitioning north of the fault are evidently similar in orientation to those responsible for folding on east-southeast axes south of the fault (Fig. 1).

The slip rate of the Altyn Tagh fault inferred from the geodetic data (Fig. 5) is 2–4 times lower than that inferred from the offset of Holocene post-glacial features[3] and from ^{14}C dating of 6 kyr BP morphological features offset by the surface fault[5]. Although the GPS data may be questioned for their low signal-to-noise ratio (4:1), we note that the slow slip rate is largely responsible for this low ratio. We believe that systematic control-point instability does not artificially lower our GPS estimate because the fault-normal GPS data are consistent with the fault-normal contraction rate inferred independently from the levelling data. Moreover, our slow slip-rate on the Altyn Tagh fault is consistent with comparable slow convergence across the eastern edge of the Tibetan plateau[20] and with the net velocities of Altyn Tagh displacements relative to Eurasia (see inset to Fig. 1). These velocities were derived by adding velocities relative to Lhasa to the velocity of Lhasa relative to Eurasia[21], and correcting for the rotation of Eurasia in the GPS frame of reference. In this Eurasia-fixed projection, sites southeast of the Altyn Tagh fault have a small eastward motion relative to Eurasia (5 ± 3 mm yr^{-1}), while sites northwest of the fault have a small westward motion with similar rate.

At 87–91° E, contraction between northern India and Urumqi in the northern Tien Shan amounts to 33.5 ± 5 mm yr^{-1}, of which 20.3 ± 3 mm yr^{-1} occurs across the Himalaya[22], 9 ± 2 mm yr^{-1} across Tibet, 2.5 ± 1.5 mm yr^{-1} across the Altyn Tagh system and 2 ± 3 mm yr^{-1} across the southeastern Tien Shan. Thus, in contrast to some interpretations of Asian kinematics in which the Altyn Tagh fault absorbs one-third of the entire Indo-Asian convergence signal, the system apparently absorbs less than 10%. The minor contraction we find in the eastern Tien Shan at 90° E, when compared with the inferred 20 mm yr^{-1} north–south contraction of the western Tien Shan[23], requires the Tarim basin to rotate clockwise relative to Eurasia at approximately 1° per Myr, a rate that must apply also to the clockwise rate of change of strike of the Altyn Tagh fault[24].

Although the geodetic slip rate and convergence on the Altyn Tagh system reported here is interpreted in the context of the

Table 1 Coordinates and velocities of GPS points relative to MANG

Site	Latitude (°N)	Longitude (°E)	Slip rate north (mm yr^{-1})	Slip rate east (mm yr^{-1})
URUR	43.81424	87.7051	− 1.6 ± 2.8	− 3.3 ± 1.2
KULA	41.81643	86.19112	1.4 ± 5.0	2.1 ± 2.2
LOBU	39.44595	88.26519	− 5.0 ± 3.5	− 1.2 ± 1.6
MILA	39.24141	88.89869	− 7.6 ± 3.2	− 3.7 ± 1.5
KUMU	38.84900	89.14083	− 8.4 ± 3.3	− 4.4 ± 1.5
PAXI	38.61399	89.28199	− 14.9 ± 3.5	− 12.6 ± 1.6
NICE	38.46829	89.63004	− 8.5 ± 4.4	− 3.6 ± 1.9
KLSA	38.40933	89.90475	− 3.2 ± 3.4	− 0.9 ± 1.5
SCAN	38.40854	89.92951	2.7 ± 4.6	− 3.0 ± 2.2
SCAS	38.40388	89.93227	− 4.7 ± 5.3	− 1.4 ± 2.9
HAPI	38.39144	89.96822	− 4.9 ± 3.4	− 0.9 ± 1.5
TERR	38.39113	90.08462	− 1.4 ± 2.9	0.6 ± 1.2
MULI	38.37611	90.41844	− 1.2 ± 3.2	− 0.3 ± 1.5
HATU	38.28494	90.90676	− 2.9 ± 3.1	− 1.6 ± 1.4
MANG	37.88704	91.82126	0	0

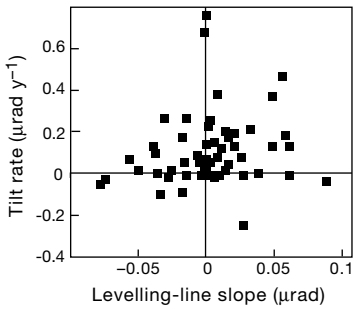

Figure 3 Plot of slope versus tilt-rate between adjacent bench marks. No clear correlation is shown, indicating a probable absence of significant systematic levelling errors.

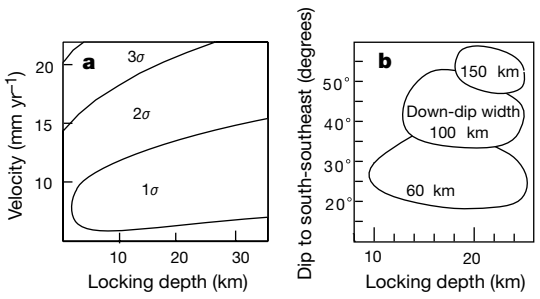

Figure 4 Solution-space contours for the dislocation models illustrated in Fig. 2. **a**, Weighted least-squares misfits to GPS observations (1–3σ). **b**, Weighted least-squares misfits to the levelling data for various locking-depths, dips, down-dip widths and slip rates.

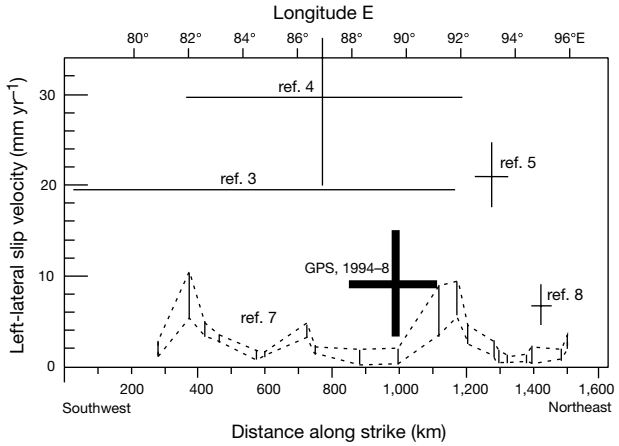

Figure 5 Dextral slip rate estimates for the Altyn Tagh fault. The geological estimates from the State Seismological Bureau[7] indicate the range of reported values, all of which are likely to represent lower bounds. The GPS error cited is 1σ from Fig. 4a.

localized deformation implicit in kinematic reconstructions of Asian tectonics, models that incorporate Altyn Tagh slip rates faster than 15 mm yr^{-1} are inconsistent with recent GPS data. The absence of a closer agreement between current GPS rates and slip rates averaged over many thousands of years is puzzling, and if we assume each estimate to be free from error, would require a secular slowing in slip rate. The low rates reported here support the view that Tibet is currently not being extruded rapidly to the east[13,25] and requires a larger portion of Indo-Asian convergence to be absorbed by faults elsewhere, or by internal deformation of structural units in Asia. Our findings of a low rate of shear strain on the northern margin of Tibet, and slow northward contraction and eastward extension[26] of the Tibetan plateau at a strain of approximately 10^{-8} yr^{-1} are similar to those predicted by dynamic models for Indo-Asian convergence. □

Received 13 August; accepted 9 December 1999.

1. Molnar, P. & Tapponnier, P. Cenozoic tectonics of Asia: Effects of a continental collision. *Science* **189,** 419–426 (1975).
2. Molnar, P. & Deng, Q. Faulting associated with large earthquakes and the average rate of deformation in central and eastern Asia. *J. Geophys. Res.* **89,** 6203–6228 (1984).
3. Peltzer, G., Tapponier, P. & Armijo, R. Magnitude of Late Quaternary left-lateral displacements along the north edge of Tibet. *Science* **246,** 1285–1289 (1989).
4. Avouac, J-P. & Tapponier, P. Kinematic model of active deformation in central Asia. *Geophys. Res. Lett.* **20,** 895–898 (1993).
5. Meriaux, A. *et al.* Large-scale strain patterns, great earthquakes, and late Pleistocene slip-rate along the Altyn Tagh fault (China). *Eos* (Fall Meet. Suppl.) **79,** 400 (1998).
6. Houseman, G. & England, P. Finite strain calculations of continental collision. 1. Methods and general results for convergent zones. *J. Geophys. Res.* **91,** 3651–3663 (1986).
7. *Altyn Tagh Fault* 1–353 (Special Publication, Seismological Bureau of China, Beijing, 1992). (In Chinese.)
8. Meyer, B. *et al.* Rate of left-lateral movement along the easternmost segment of the Altyn Tagh Fault, east of 96° E China. *Geophys. J. Int.* **124,** 29–44 (1996).
9. Lamb, S. A simple method for estimating the horizontal velocity field in wide zones of active deformation—II. Examples from New Zealand, Central Asia and Chile. *Geophys. J. Int.* **119,** 313–377 (1994).
10. Peltzer, G. & Saucier, F. Present-day kinematics of Asia derived from geologic fault rates. *J. Geophys. Res.* **101,** 27943–27956 (1996).
11. Vilotte, J., Daignieres, M. & Madariaga, R. Numerical modeling of intraplate deformation: simple mechanical models of continental collision. *J. Geophys. Res.* **87,** 10709–10728 (1982).
12. Kong, X. & Bird, P. in *Tectonic Evolution of Asia* (eds Yin, A. & Harrison, T. M.) 18–34 (Cambridge Univ. Press, 1996).
13. Houseman, G. & England, P. Crustal thickening versus lateral expulsion of Tibet. *J. Geophys. Res.* **98,** 12233–12249 (1993).
14. England, P. & Molnar, P. Active deformation of Asia: from kinematics to dynamics. *Science* **278,** 647–650 (1997).
15. Jackson, M. & Bilham, R. Constraints on himalayan deformation inferred from vertical velocity fields in Nepal and Tibet. *J. Geophys. Res.* **99,** 13897–13912 (1994).
16. Larson, K., Freymueller, J. & Philipsen, S. Global plate velocities from the Global Positioning System. *J. Geophys. Res.* **102,** 9961–9982 (1997).
17. Savage, J. Displacement field for an edge dislocation in a layered half-space. *J. Geophys. Res.* **103,** 2439–2446 (1998).
18. McCaffrey, R. in *Tectonic Evolution of Southeast Asia* (eds Hall, R. & Blundell, D. J.) Vol. 106, 3–18 (Geol. Soc. Lond. Spec. Pub., 1996).
19. Jones, C. & Wesnousky, S. Variations in strength and slip rate along the San Andreas fault system. *Science* **256,** 83–86 (1992).
20. King, R. W. *et al.* Geodetic measurement of crustal motion in southwest China. *Geology* **25,** 179–182 (1997).
21. Larson, K., Bürgmann, R., Bilham, R. & Freymueller, J. Kinetics of the India-Eurasia collision zone from GPS measurements. *J. Geophys. Res.* **104,** 1111–1130 (1999).
22. Bilham, R., Larson, K., Freymueller, J. & Project Idylhim members. GPS measurements of present-day convergence across the Nepal Himalaya. *Nature* **386,** 61–64 (1997).
23. Abdrakhmatov, K. *et al.* Relatively recent construction of the Tien Shan inferred from GPS measurements of present-day crustal deformation rates. *Nature* **384,** 450–453 (1996).
24. Longjun, Y. & Liou, J. G. Two stage evolution model for the Altyn Tagh fault, China. *Geology* **27,** 227–230 (1999).
25. England, P. & Molnar, P. Right-lateral shear and rotation as the explanation for strike slip faulting in Eastern Tibet. *Nature* **344,** 140–142 (1990).
26. Bilham, R., Blume, F., Bendick, R. & Gaur, V. Geodetic constraints on the translation and deformation of India: Implications for future great Himalayan earthquakes. *Curr. Sci.* **74,** 213–229 (1998).

Acknowledgements

The investigations were funded by the National Science Foundation. G. Pelzer participated in the 1994 survey and we thank him and G. King, P. Tapponnier, P. England, and P. Molnar for discussions of the Asian collision process. R.B. received a John Simon Guggenheim Memorial Foundation fellowship while at Oxford University.

Correspondence and requests for materials should be addressed to R.B. (e-mail: bilham@stripe.colorado.edu).

Tree species impoverishment and the future flora of the Atlantic forest of northeast Brazil

José Maria Cardoso da Silva* **& Marcelo Tabarelli†**

** Universidade Federal de Pernambuco, Centro de Ciências Biológicas, Departamento de Zoologia, Av. Prof. Moraes Rego 1235, 50670-020, Recife, PE, Brazil*
† Universidade Federal de Pernambuco, Centro de Ciências Biológicas, Departamento de Botánica, Av. Prof. Moraes Rego 1235, 50670-020, Recife, PE, Brazil

Estimates of species extinction due to human impact on tropical forests have previously been based on the relationship between species number and area[1]. Here we use a different approach to estimate loss of tree species in the Atlantic forest of northeast Brazil. We evaluate the characteristics of plant species, their avian dispersers and the distribution of the forest remnants on the landscape to estimate that about 33.9% of tree species in this region will become extinct on a regional scale. Because northeast Brazil is the most threatened sector of South American Atlantic forest[2], our results highlight the need to change the current conservation paradigm for this region. Rather than focus on the creation of isolated reserves in any medium-to-large forest remnant, a bioregional planning approach is urgently required to rescue this unique biota from extinction.

The Atlantic forest of northeast Brazil includes all forests located north of the River São Francisco. This 35,625.92 km^2 region has been identified as an important area of endemism in South America[3,4]. Its biota is influenced by the Amazonian region, making it very distinctive from other sectors of the Atlantic forest[4]. In northeast Brazil, most of the Atlantic forest has been converted into agricultural land, with only 2% of the original forest remaining[5,6]. Forest remnants are dispersed as small patches surrounded by open fields[6]. Protected areas in this region are mostly small, isolated and badly managed[2]. Also, hunting pressure on the fauna of these fragments is very high[7].

Tropical forests distributed in similar landscapes to northeast Brazil are losing plant species through the disruption of key ecological processes such as pollination and seed dispersal[8]. However, no estimates of the number of threatened plant species have been made. Pollination and seed dispersal are critical because they directly affect the reproductive success of plants, and in tropical species they usually involve direct interaction with animals[9,10]. Thus, habitat loss affects tree species through its effects on the plants themselves, on their pollinators and dispersers, or on both[11].

We recorded 427 tree species in the Atlantic forest of northeast Brazil. A total of 305 (71.4%) species were dispersed by vertebrates (mostly birds and mammals). Species classified as dispersed by abiotic factors represented 28.5% (122) of the total pool. We obtained data about niche regeneration for 289 species dispersed by vertebrates. Most of these (206) had fruits smaller than 15 mm. In this group, 101 (49.0%) were shade-intolerant and 93 (45.1%) were shade-tolerant species. This difference is not significant ($\chi^2 = 0.33$, $P < 0.05$). However, of the 95 vertebrate-dispersed species with fruits larger than 15 mm, there were significantly more species classified as shade-tolerant (66) than shade-intolerant (25) ($\chi^2 = 18.15$; $P < 0.002$).

A total of 78 fruit-eating birds were recorded in the region. Of these, 59 had gapes narrower than 15 mm and 19 had gapes wider than 15 mm. This difference is significant ($\chi^2 = 19.7$; $P < 0.05$). Of the species with narrow gapes, most of them (31) were edge rather than forest (28) species, but this difference is not significant ($\chi^2 = 0.15$; $P > 0.05$). A different pattern is found among species with gapes wider than 15 mm, where there were significantly more